




## Quench-induced dynamical topology under dynamical noise

Lin Zhang <sup>1,2</sup> Long Zhang <sup>1,2</sup> and Xiong-Jun Liu <sup>1,2,3,4,\*</sup>

<sup>1</sup>International Center for Quantum Materials and School of Physics, Peking University, Beijing 100871, China

<sup>2</sup>Collaborative Innovation Center of Quantum Matter, Beijing 100871, China

<sup>3</sup>CAS Center for Excellence in Topological Quantum Computation, University of Chinese Academy of Sciences, Beijing 100190, China

<sup>4</sup>Institute for Quantum Science and Engineering and Department of Physics, Southern University of Science and Technology, Shenzhen 518055, China



(Received 15 May 2020; accepted 23 February 2021; published 10 March 2021)

Equilibrium topological phases are robust against weak static disorder but may break down in the strong-disorder regime. Here we propose to explore how the quench-induced emergent dynamical topology evolves under dynamical noise and uncover novel dynamical topological physics beyond equilibrium counterparts. We develop an analytic theory and show that for weak noise, the quantum dynamics induced by quenching an initial trivial phase to the Chern insulating regime exhibits robust emergent topology on certain momentum subspaces called band-inversion surfaces (BISs). The dynamical topology is protected by the minimal oscillation frequency over BISs, mimicking a bulk gap of the dynamical phase. Two novel types of dynamical transitions classified by distinct exceptional points or rings are predicted if increasing the noise to critical strength, with critical points being exactly obtained. At the exceptional points on the BISs the minimal oscillation frequency vanishes, manifesting the dynamical bulk-gap closing, beyond which the dynamical topology breaks down. Interestingly, we predict a *sweet spot* region of the transition, in which the dynamical topology survives surprisingly at an arbitrarily strong noise regime. This work unveils novel universal physics of dynamical topology under dynamical noise, which can be probed with control in experiment.

DOI: [10.1103/PhysRevResearch.3.013229](https://doi.org/10.1103/PhysRevResearch.3.013229)

### I. INTRODUCTION

The topological quantum phases [1–6] are defined on the ground state of a system in equilibrium with a nontrivial bulk topological invariant, and host topologically protected gapless boundary modes through the celebrated bulk-boundary correspondence [5,6]. Since their discovery, the topological quantum phases have ignited extensive research in condensed matter physics [7–10], photonic systems [11–14], and ultracold atoms [15–21], with the focus mainly on the equilibrium properties, such as the classification [22–24] and the search, synthesis, and detection in real materials [25–29]. Although these studies have led to tremendous progress, a full and comprehensive understanding of the underlying topological physics remains incomplete, especially about their nonequilibrium properties.

Recently, benefiting from the advances in quantum simulations which provide a fully controllable platform to realize various topological phases [17–21], considerable efforts have been devoted to investigate the topological physics out of equilibrium [30–41]. Particularly, by quenching a  $d$ -dimensional ( $dD$ ) topological system, nontrivial dynamical

topological patterns are predicted to emerge on the  $(d - 1)D$  momentum subspaces called band-inversion surfaces (BISs) in quantum dynamics, which universally correspond to the bulk topology of the  $dD$  equilibrium topological phase [42–48]. This dynamical bulk-surface correspondence provides new schemes to characterize and detect the equilibrium topological phase via nonequilibrium quench dynamics, and has been generalized to various topological systems [49–53], with the experimental verifications having been widely reported recently [54–60].

On the other hand, the dynamical bulk-surface correspondence opens a way to classify nonequilibrium quantum dynamics with topological theory. The nontrivial topological patterns emerging on the BISs manifest a new notion of dynamical topological phases, which are connected to but conceptually different from the equilibrium counterparts, with the underlying nontrivial physics remaining to be unearthed. For example, it is known that the equilibrium topological phases are robust against weak static disorder but may break down in the strong-disorder regime [61–63]. The disorder effect may also give rise to the topological Anderson insulators [64–66]. Being a temporal analogy to the spatial static disorder, the dynamical noise obviously destroys the equilibrium topological phase. However, is the emergent dynamical topology in quantum quenches robust against dynamical noise? Does the dynamical topological transition occur, and how does it occur, under the strong-noise regime? How should we classify such dynamical transitions? Is there any novel feature beyond the equilibrium topology? Although the dynamical noise indeed exists and is inevitable in practical experiments

\*Corresponding author: [xiongjunliu@pku.edu.cn](mailto:xiongjunliu@pku.edu.cn)

Published by the American Physical Society under the terms of the [Creative Commons Attribution 4.0 International](https://creativecommons.org/licenses/by/4.0/) license. Further distribution of this work must maintain attribution to the author(s) and the published article's title, journal citation, and DOI.

[54–60], these novel issues have not been studied either theoretically or experimentally. Answering these questions will promote the basic understanding of the emergent dynamical topological phases in quantum quenches and stimulate experimental studies of their exceptional features with controllable noise.

In this work, we address these issues by investigating the quench-induced dynamical topology under dynamical noise for 2D quantum anomalous Hall (QAH) systems. The analytic theory of the quench dynamics is developed based on the stochastic Schrödinger equation. In the weak-noise regime, we show that the dynamical topology emerging on the dynamical band-inversion surfaces (dBISs) is protected by the minimal oscillation frequency which mimics the bulk gap of the emergent dynamical phase. In the strong-noise regime, the exceptional points emerge in the dynamical patterns on dBISs and the dynamical topology breaks down. Interestingly, we uncover two types of dynamical topological transitions classified by distinct exceptional points or rings, with critical points being exactly obtained. Moreover, we predict a *sweet spot* region, in which the dynamical topology survives surprisingly at arbitrary strong noise. This result is beyond the equilibrium counterparts.

The paper is organized as follows. In Sec. II, we introduce the QAH model with dynamical noise and discuss the corresponding dissipative quench dynamics. In Sec. III, we generalize the emergent dynamical topology into the dissipative regime. In Sec. IV, we study the stability of the emergent dynamical topology under weak noise. The dynamical transitions in the strong-noise regime are discussed in Sec. V. Further, in Sec. VI we show the critical noise strength and the sweet spot region. Finally, we present the conclusion and outlook in Sec. VII. More details are provided in the appendices.

## II. NOISE-INDUCED DISSIPATIVE QUENCH DYNAMICS

We start with 2D QAH models coupling to dynamical white noise, with the Hamiltonian

$$\tilde{H}(\mathbf{k}, t) = H(\mathbf{k}) + \mathbf{w}(\mathbf{k}, t) \cdot \boldsymbol{\sigma} + \delta m_z(t) \sigma_z, \quad (1)$$

where  $H(\mathbf{k}) = \mathbf{h}(\mathbf{k}) \cdot \boldsymbol{\sigma}$  gives the QAH phase, and  $w_i(\mathbf{k}, t)$  is magnetic white noise of strength  $\sqrt{w_i}$ , which exists and is also controllable in experiments [54–58], satisfying  $\langle w_i(\mathbf{k}, t) \rangle = 0$  and  $\langle w_i(\mathbf{k}, t) w_j(\mathbf{k}, t') \rangle = w_i \delta_{ij} \delta(t - t')$ . Here  $\langle \cdot \rangle$  denotes the stochastic average over different noise configurations. We tune the magnetization  $\delta m_z$  to trigger the quench dynamics from the deep trivial state to the topologically nontrivial phase; see Fig. 1(a). For  $t < 0$ , we set  $\delta m_z \ll 0$  such that the system is initially prepared in the fully polarized state  $|\psi(\mathbf{k}, t=0)\rangle = |\uparrow\rangle$  and the noise is negligible for the prequench state. Quenching  $\delta m_z \rightarrow 0$  at  $t = 0$  leads to evolution under the postquench Hamiltonian with noise  $H_{\text{post}}(\mathbf{k}, t) = H(\mathbf{k}) + \mathbf{w}(\mathbf{k}, t) \cdot \boldsymbol{\sigma}$ . The dynamics is governed by the stochastic Schrödinger equation [67–70],  $i\partial_t |\psi(\mathbf{k}, t)\rangle = H_{\text{post}}(\mathbf{k}, t) |\psi(\mathbf{k}, t)\rangle$ , a noise-induced random unitary evolution. Our study can be readily generalized to quench dynamics along an arbitrary axis [42] and from a generic trivial state [44].

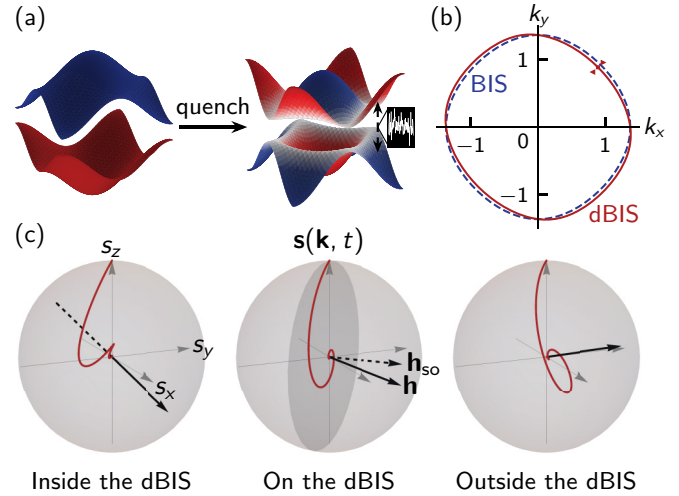


FIG. 1. Noise-induced dissipative quench dynamics and the dynamical band-inversion surfaces. (a) Quenching a 2D QAH model from deep trivial state to the topologically nontrivial regime. The white noise (the insert) randomly couples the upper and lower bands. (b) The dBIS (red line) and BIS (dashed blue line). (c) The stochastic averaged spin polarizations  $\mathbf{s}(\mathbf{k}, t)$  for the momenta marked in (b) by red triangles. On the dBIS, the evolution of spin polarization (red line) is always within the plane perpendicular to the SO axis  $\mathbf{h}_{\text{so}}$  (black dashed arrow), while it spirals around the postquench Hamiltonian vector  $\mathbf{h}$  (black arrows) for momenta off the dBIS (including the BIS). Here we set  $m_z = 1.2t_0$  and  $t_{\text{so}} = 0.2t_0$  for the postquench Hamiltonian. The noise strength is  $w_x = 0.12t_0$ ,  $w_y = 0$ ,  $w_z = 0.02t_0$ .

The quench dynamics with noise can be quantified by the stochastic averaged spin polarization

$$\mathbf{s}(\mathbf{k}, t) \equiv \langle \langle |\psi(\mathbf{k}, t)\rangle \boldsymbol{\sigma} |\psi(\mathbf{k}, t)\rangle \rangle. \quad (2)$$

The random evolution of spin polarization renders the dissipative quantum dynamics [Fig. 1(c)], which can be obtained from the Lindblad master equation [69–71] for the stochastic averaged density matrix  $\mathbf{s}(\mathbf{k}, t) = \text{Tr}[\rho(\mathbf{k}, t)\boldsymbol{\sigma}]$ , with  $\rho(\mathbf{k}, t) = \langle |\psi(\mathbf{k}, t)\rangle \langle \psi(\mathbf{k}, t)| \rangle$  and

$$\partial_t \rho(\mathbf{k}, t) = \mathcal{L}_{\mathbf{k}}[\rho(\mathbf{k}, t)], \quad \partial_t \mathbf{s}(\mathbf{k}, t) = \mathcal{L}(\mathbf{k})\mathbf{s}(\mathbf{k}, t). \quad (3)$$

Here the Liouvillian superoperator reads  $\mathcal{L}_{\mathbf{k}}[\bullet] \equiv -i[H(\mathbf{k}), \bullet] + \sum_{i=x,y,z} w_i [\sigma_i \bullet \sigma_i - \bullet]$  and can be recast into the following matrix form for the two-band model with  $\rho(\mathbf{k}, t) = [1 + \mathbf{s}(\mathbf{k}, t) \cdot \boldsymbol{\sigma}]/2$ :

$$\mathcal{L}(\mathbf{k}) = 2 \begin{bmatrix} -w_y - w_z & -h_z(\mathbf{k}) & h_y(\mathbf{k}) \\ h_z(\mathbf{k}) & -w_x - w_z & -h_x(\mathbf{k}) \\ -h_y(\mathbf{k}) & h_x(\mathbf{k}) & -w_x - w_y \end{bmatrix}, \quad (4)$$

where the noise  $w_j$  is directly coupled to spin components  $s_i$  ( $i \neq j$ ) for its dephasing effect in the basis  $|\sigma_j\rangle$ . The noise in general couples the eigenstates of  $H(\mathbf{k})$ , leading to a decay effect instead of pure dephasing and modulating the oscillation frequency. The same master equation can be reached for quantum noise [72], so this study is applicable to the case with quantum noise.

By diagonalizing the Liouvillian superoperator  $\mathcal{L}(\mathbf{k})$ , the solution to the dissipative quench dynamics can be generically

written as

$$\begin{aligned} \mathbf{s}(\mathbf{k}, t) = & \mathbf{s}_0(\mathbf{k})e^{-\lambda_0(\mathbf{k})t} + \mathbf{s}_+(\mathbf{k})e^{-[\lambda_+(\mathbf{k})+i\omega(\mathbf{k})]t} \\ & + \mathbf{s}_-(\mathbf{k})e^{-[\lambda_-(\mathbf{k})-i\omega(\mathbf{k})]t}, \end{aligned} \quad (5)$$

with the coefficients  $s_\alpha(\mathbf{k}) = [s_\alpha^L(\mathbf{k}) \cdot \mathbf{s}(\mathbf{k}, 0)]s_\alpha^R(\mathbf{k})$  for  $\alpha = 0, \pm$ . Here  $s_\alpha^{L(R)}$  satisfying  $s_\alpha^L(\mathbf{k}) \cdot s_\beta^R(\mathbf{k}) = \delta_{\alpha\beta}$  are the left (right) eigenvectors of the Liouvillian superoperator

$$\mathcal{L}^T(\mathbf{k})s_\alpha^L = -\lambda_\alpha s_\alpha^L, \quad \mathcal{L}(\mathbf{k})s_\alpha^R = -\lambda_\alpha s_\alpha^R, \quad (6)$$

with eigenvalues  $\lambda_0$  and  $\lambda_\pm = \lambda_1 \pm i\omega$ , respectively, and  $s_0^{L(R)}$  are real. The coefficients  $\lambda_{0,1}$  reflect explicitly the dissipation of the spin dynamics due to the dynamical noise. Note that  $\omega$  may become imaginary for certain noise strength, manifesting a fully decayed spin dynamics. The above formal solution is valid only for momenta with three distinct eigenvalues, which, however, does not affect the analysis of dynamical topology.

### III. EMERGENT DYNAMICAL TOPOLOGY

As is known that without noise, the nontrivial topology emerges in the quench dynamics on BISs where the spin-flip resonant oscillations occur and thus the time-averaged spin-polarization vanishes  $\overline{s(\mathbf{k})} \equiv \lim_{T \rightarrow \infty} \frac{1}{T} \int_0^T dt \mathbf{s}(\mathbf{k}, t)|_{\mathbf{k} \in \text{BIS}} = 0$  [42–44]. This characterization needs generalization in the noise regime, when the decay dominates the long-time evolution and the direct time-averaging  $\overline{s(\mathbf{k})}$  vanishes at any  $\mathbf{k}$ , hence does not capture the topology. Below we first extend the characterization theory to the generic case with dissipation.

For unitary quench dynamics, the BISs correspond to the momentum subspace  $\{\mathbf{k}|h_z(\mathbf{k}) = 0\}$  with  $\mathbf{h}(\mathbf{k}) \cdot \mathbf{s}(\mathbf{k}, 0) = 0$ , where the spin processes perpendicularly to spin-orbit (SO) axis  $\mathbf{h}_{\text{so}}(\mathbf{k}) = (h_x, h_y)$ . With dynamical noise, on such BISs the spin dynamics are complicated. However, we show that on the  $\mathbf{k}$ -subspace dubbed dBISs defined by  $s_0^L$  as

$$\text{dBIS} \equiv \{\mathbf{k}|s_0^L(\mathbf{k}) \cdot \mathbf{s}(\mathbf{k}, 0) = 0\}, \quad (7)$$

under noise the spin processes fully in the plane perpendicular to the SO axis  $\mathbf{h}_{\text{so}}$  (see Appendix A). Away from the dBISs, the spin evolves along a generic 3D curve in the Bloch sphere. For the initial state  $|\uparrow\rangle$ , the dBISs are analytically given by the momenta satisfying  $h_z = (w_y - w_x)h_x h_y / (h_x^2 + h_y^2)$  with  $s_0^L \sim (h_x, h_y, 0)$ . The dBISs return to the BISs if the noise strengths are zero or  $w_x = w_y$ . The numerical results in Fig. 1 confirm features on the dBIS, where we consider the QAH model [16,73] realized in recent experiments [21,74],  $H(\mathbf{k}) = \mathbf{h}(\mathbf{k}) \cdot \boldsymbol{\sigma}$  with  $\mathbf{h}(\mathbf{k}) = (t_{\text{so}} \sin k_x, t_{\text{so}} \sin k_y, m_z - t_0 \cos k_x - t_0 \cos k_y)$ , where  $t_0$  and  $t_{\text{so}}$  denote the spin-conserved and spin-flipped hopping. The magnetization  $m_z$  is suddenly changed from a large negative value to  $m_z = 1.2t_0$  [Fig. 1(a)], together with  $t_{\text{so}} = 0.2t_0$ ,  $w_x = 0.12t_0$ ,  $w_y = 0$ , and  $w_z = 0.02t_0$ . The dBIS differs from the BIS even when the noise is weak [Fig. 1(b)]. On the dBIS, the spin polarization evolves exactly within the plane perpendicular to  $\mathbf{h}_{\text{so}}$ , but not for momenta off the dBIS [including the BIS; see Fig. 1(c)].

The emergent topology characterizes the global feature of the dynamical spin texture which is normalized [42]. For this we can neglect the amplitude decay (quantified by  $\text{Re } \lambda_\alpha$ ) of the spin polarization to characterize the dynamical topology,

except for the case with singularities, giving the rescaled dynamical spin polarization [75]

$$\tilde{\mathbf{s}}(\mathbf{k}, t) \equiv \mathbf{s}_0(\mathbf{k}) + \mathbf{s}_+(\mathbf{k})e^{-i\omega(\mathbf{k})t} + \mathbf{s}_-(\mathbf{k})e^{+i\omega(\mathbf{k})t}. \quad (8)$$

This characterization requires the frequency  $\omega(\mathbf{k})$  to be real. Otherwise, spin dynamics is characterized by purely decay, as dominated by the noise, and the information of the postquench topological Hamiltonian is scrambled for the indistinguishable decay modes with real  $\lambda_\alpha$ 's. The emergent topology of the quench dynamics is characterized by the topological invariant

$$\mathcal{W} \equiv \frac{1}{2\pi} \oint_{\text{dBIS}} \mathbf{g}(\mathbf{k}) d\mathbf{g}(\mathbf{k}). \quad (9)$$

Here  $\mathbf{g}(\mathbf{k})$  denotes the directional derivative of dynamical spin polarization in  $x$ - $y$  plane  $\mathbf{g}(\mathbf{k}) \equiv (1/\mathcal{N}_{\mathbf{k}})\partial_{k_\perp}(\tilde{s}_x(\mathbf{k}), \tilde{s}_y(\mathbf{k}))|_{\text{dBIS}}$  normalized by  $\mathcal{N}_{\mathbf{k}}$ , with  $k_\perp$  perpendicular to the dBISs and pointing to the side with  $s_0^L(\mathbf{k}) \cdot \mathbf{s}(\mathbf{k}, 0) > 0$ . The invariant  $\mathcal{W}$  represents the winding number of  $\mathbf{g}(\mathbf{k})$  over dBISs. This invariant naturally returns to the one for unitary quench dynamics if the noise is absent, which characterizes the topological phase of the postquench Hamiltonian [42,44].

### IV. STABILITY OF THE DYNAMICAL TOPOLOGY

Now we study the fate of dynamical topology under dynamical noise, and consider first the weak-noise regime with the spin dynamics on dBISs exhibiting damped oscillation. Accordingly  $\tilde{\mathbf{s}}(\mathbf{k}, t)$  on the dBISs oscillate around zero [see Fig. 2(a)], leading to vanishing time averaged spin polarization  $|\overline{\tilde{\mathbf{s}}(\mathbf{k})}|_{\mathbf{k} \in \text{dBISs}} = 0$ ; see Fig. 2(b). Near the dBISs, for the real and nonzero oscillation frequency  $\omega(\mathbf{k})$  we have  $\overline{\tilde{\mathbf{s}}(\mathbf{k})} = \mathbf{s}_0(\mathbf{k})$ . It follows that the dynamical field is obtained by  $\mathbf{g}(\mathbf{k}) = \frac{1}{\mathcal{N}_{\mathbf{k}}}(s_{0,x}^R(\mathbf{k}), s_{0,y}^R(\mathbf{k}))|_{\text{dBIS}}$  and explicitly reads (see Appendix A)

$$\mathbf{g}(\mathbf{k}) = \frac{1}{\mathcal{N}_{\mathbf{k}}}(h_x(\mathbf{k})[1 - \eta(\mathbf{k})], h_y(\mathbf{k})[1 + \eta(\mathbf{k})])|_{\text{dBIS}}, \quad (10)$$

where the deformation factor is  $\eta = [(w_y - w_x)/\mathbf{h}_{\text{so}}^2] \times (w_x h_x^2/\mathbf{h}_{\text{so}}^2 + w_y h_y^2/\mathbf{h}_{\text{so}}^2 - w_z)$ . The factor  $\eta$  quantifies the deformation of  $\mathbf{g}(\mathbf{k})$  from the SO field  $\mathbf{h}_{\text{so}}$ . It is seen that the noise cannot fully flip  $\mathbf{g}$  with respect to  $\mathbf{h}_{\text{so}}$ , which is crucial for the robustness of dynamical topology in the relatively weak noise regime. Finally, for the case with  $w_x = w_y$  or without noise, the SO field is recovered. These results are valid in general for the damped oscillating spin dynamics on the dBISs.

The stability of dynamical topology under weak noise can be examined by increasing the noise strength from zero. Without noise, the invariant  $\mathcal{W}$  reduces to the winding of SO field  $\mathbf{h}_{\text{so}}$  on the BISs, which is clearly nontrivial. As the noise increases to the weak regime, no topological charge with  $\mathbf{h}_{\text{so}}(\mathbf{k}) = 0$  passes through the deformed dBISs (see Appendix B). Thus the winding of the SO field  $\mathbf{h}_{\text{so}}$  on the dBISs remains invariant. In Appendix B, we prove that while the  $\mathbf{g}(\mathbf{k})$  field on the dBISs is locally deformed by the noise, its global topology, quantified by  $\mathcal{W}$ , is unchanged and still equivalent to that of the SO field  $\mathbf{h}_{\text{so}}$ , as long as dissipative spin dynamics has finite minimal oscillation frequency over the dBISs, which mimics a bulk gap protecting the emergent dynamical phase against relatively weak noise. In Fig. 2(c),

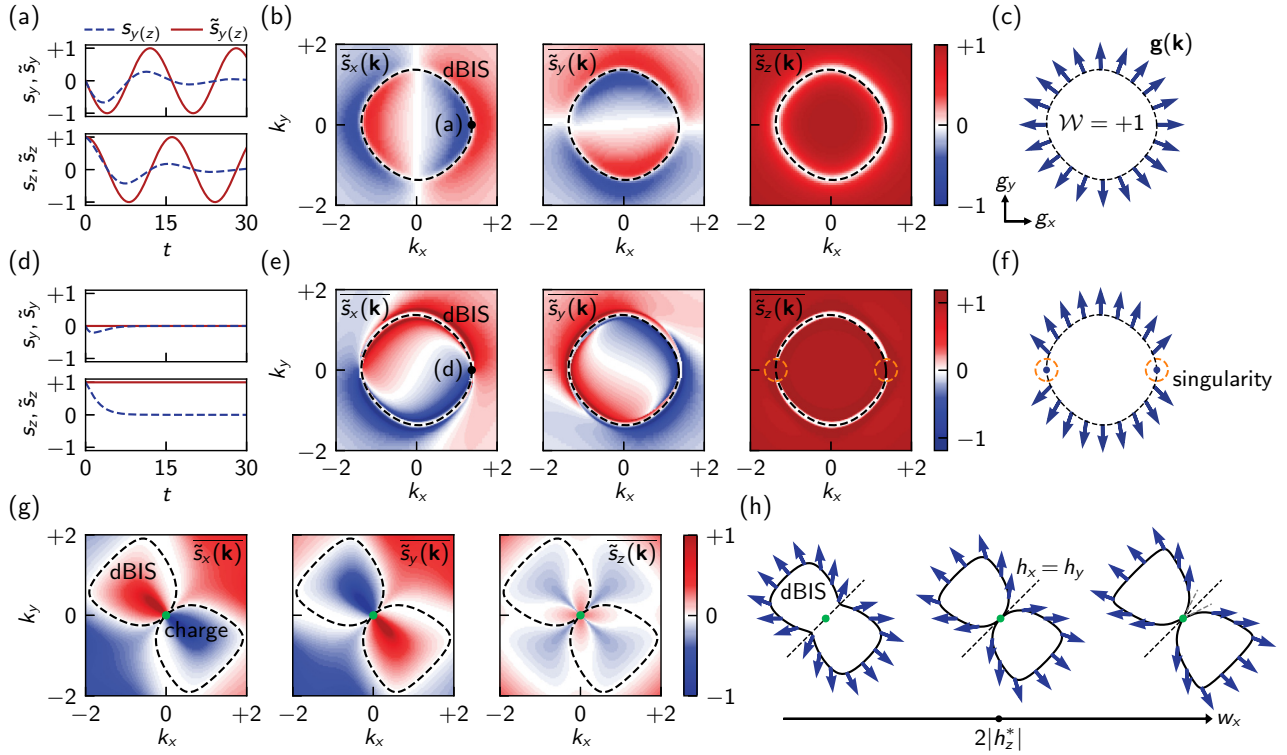


FIG. 2. Two types of dynamical topological transition. (a) The rescaled dynamical spin polarization  $\tilde{s}(t)$  (red lines) and spin polarization  $s(t)$  (dashed blue lines) on dBIS momentum with  $k_y = 0$  marked by the black dot in (b). The corresponding components  $s_x, \tilde{s}_x$  are always zero. (b) The time-averaged rescaled spin polarizations  $\tilde{s}(\mathbf{k})$  under weak noise strength  $w_x = 0.05t_0, w_y = 0, w_z = 0.01t_0$ . The vanishing time averages  $\tilde{s}(\mathbf{k}) = 0$  characterize the dBIS (dashed line). (c) The dynamical pattern  $\mathbf{g}(\mathbf{k})$  (blue arrows) exhibits nonzero topological number  $\mathcal{W} = +1$ . (d) The rescaled dynamical spin polarization and spin polarization on dBIS at the momentum marked in (e). (e) The time-averaged spin texture under strong noise strength  $w_x = 0.1t_0, w_y = 0.05t_0, w_z = 0.45t_0$ . Singularities emerge on dBIS momenta with nonzero time averaging  $\tilde{s}(\mathbf{k}) \neq 0$ . The spin dynamics at the marked momenta purely decays without oscillation. (f) The dynamical pattern  $\mathbf{g}(\mathbf{k})$  has singularities. Here we set  $m_z = 1.2t_0$  and  $t_{so} = 0.2t_0$  for (a)–(f). (g) The results for noise strength  $w_x = 1.6t_0, w_y = 0, w_z = 0.8t_0$ , where the deformed dBIS connects to the topological charge (green dot) at  $\mathbf{k} = 0$ . The dynamical topology also breaks down. Here we set  $m_z = 1.2t_0$  and  $t_{so} = 2t_0$ . (h) The variation of dynamical pattern with  $w_x$  increasing from zero while keeping  $w_y = 0$  and  $w_z = 0.8t_0$ . When  $w_x$  increases to  $2|\hbar_z^*| = 1.6t_0$ , the dBIS is deformed to the charge position where spin oscillation vanishes and the emergent topology breaks down. As  $w_x$  further increases, more dBIS momenta are deformed to charge momentum.

we show the dynamical field  $\mathbf{g}$  of the QAH model under noise strengths  $w_x = 0.05t_0, w_y = 0$ , and  $w_z = 0.01t_0$ . The quench dynamics exhibit nonzero topological number  $\mathcal{W} = +1$ .

## V. TWO TYPES OF DYNAMICAL TOPOLOGICAL TRANSITION

The quench dynamics are qualitatively different in the strong-noise regime. Two types of dynamical transitions are obtained, with numerical results shown in Figs. 2(d)–2(h). For type I, the spin dynamics at some momenta of the dBIS purely decays without oscillation [Fig. 2(d)], even though the deformation of the dBIS is relatively small. At these momenta, the eigenvalues  $\lambda_\alpha$  of  $\mathcal{L}(\mathbf{k})$  are all real; i.e.,  $\omega(\mathbf{k})$  is purely imaginary. The rescaled spin polarization  $\tilde{s}(\mathbf{k}, t) = \sum_{\alpha=0,\pm} s_\alpha(\mathbf{k}) = \mathbf{s}(\mathbf{k}, 0)$  is trivial. Thus the dBIS breaks down and the dynamical field  $\mathbf{g}(\mathbf{k})$  cannot be defined at these singular momenta in this regime [Figs. 2(e) and 2(f)]. For type II, the noise strongly deforms the dBIS to connect to topological charges. At the crossing of charges with dBISs the oscillation vanishes, leading to breakdown of the dynamical topology [Figs. 2(g) and 2(h)]. Thus the breakdown of dynamical

topology is associated with the emergence of singularities on dBISs.

These two types of dynamical transition can be further distinguished by different exceptional points or rings of the Liouvillian superoperator, consisting of exceptional momenta with  $\omega = 0$ , on which the eigenvectors  $s_\pm^{L(R)}$  coalesce. Numerically, it is more convenient to determine the exceptional momenta via the vanishing discriminant  $\Delta \equiv (bc/6 - b^3/27 - d/2)^2 + (c/3 - b^2/9)^3$  of eigenequation  $\det(\mathcal{L} + \lambda) = \lambda^3 + b\lambda^2 + c\lambda + d = 0$  (see Appendix C). The dynamical transition implies the emergence of the exceptional point on or the touch of the exceptional ring with dBISs, leading to vanishing frequency on dBISs; see Figs. 3(a) and 3(b). We show that the exceptional point or ring can be characterized by the winding number  $N_E \equiv \frac{1}{2\pi} \oint_{\mathcal{S}} d\ell \arctan \langle S_y \rangle / \langle S_x \rangle$ , where  $\mathcal{S}$  is a loop enclosing the exceptional point or ring [Figs. 3(a) and 3(b)]. Here we define  $\langle S_\alpha \rangle \equiv s_\pm^{R\dagger} S_\alpha s_\pm^R$  with  $S_\alpha$  being the spin-1 operator:

$$S_x = \begin{pmatrix} 0 & 0 & 0 \\ 0 & 0 & -i \\ 0 & i & 0 \end{pmatrix}, \quad S_y = \begin{pmatrix} 0 & 0 & i \\ 0 & 0 & 0 \\ -i & 0 & 0 \end{pmatrix}, \quad (11)$$

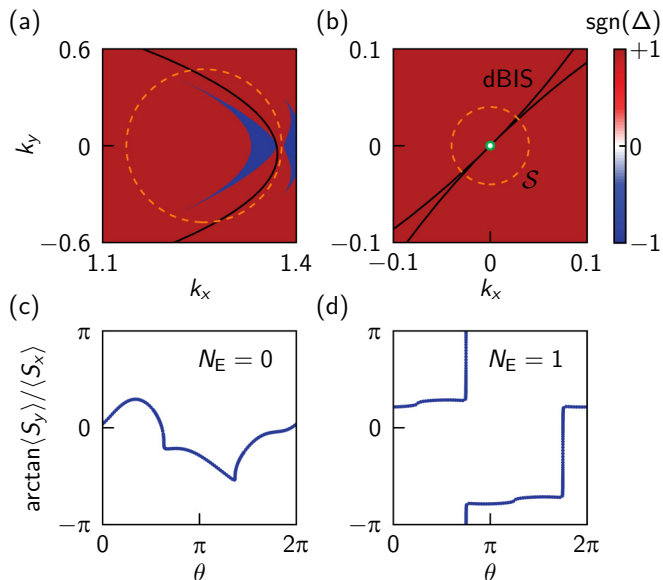


FIG. 3. Exceptional point or ring of Liouvillian superoperator. In the upper panel we plot the sign of discriminant  $\Delta$ , with exceptional momenta being given by  $\Delta = 0$ . (a) The exceptional ring (boundary of the blue cluster) touches the dBIS (black line) for type-I transition. The noise strength is  $w_x = 0.1t_0$ ,  $w_y = 0.05t_0$ , and  $w_z \approx 0.4419t_0$ . Other parameters are the same as in Figs. 2(d)–2(f). (b) The exceptional point (white dot) emerges at the charge momentum (green dot) at  $\mathbf{k} = 0$ , to which the dBIS connects for type-II transition. The noise strength is  $w_x = 1.6t_0$ ,  $w_y = 0$ , and  $w_z = 0.8t_0$ , with other parameters being the same as in Figs. 2(g) and 2(h). (c), (d) The winding of vector  $(\langle S_x \rangle, \langle S_y \rangle)$  on an ellipse loop  $\mathcal{S}$  of the form  $(x_0 + r_x \cos \theta, y_0 + r_y \sin \theta)$  [dashed orange line in (a), (b)]. The winding number  $N_E$  is trivial for type-I transition (c), but equals the charge value  $+1$  for type-II transition (d).

and  $S_z = i[S_y, S_x]$ , satisfying  $[S_\alpha, S_\beta] = i\epsilon^{\alpha\beta\gamma} S_\gamma$ . For type-I transitions, the exceptional point or ring on dBISs is characterized by a trivial winding number [Figs. 3(a) and 3(c)], while it contains the charge momentum and has a nonzero winding number  $N_E = 1$  equal to the charge value for type-II transitions [Figs. 3(b) and 3(d)]. We refer to Appendix C for more details. The distinct exceptional point or ring shows the fundamental difference between the type-I and type-II dynamical transitions.

## VI. CRITICAL NOISE STRENGTH AND SWEET SPOT REGION

The difference between the weak and strong noise regimes indicates that dynamical transitions occur at certain critical noise strengths. The dynamical topology is robust as long as the oscillation frequency of the dissipative spin dynamics is finite everywhere on dBISs; namely, the effective bulk gap of the emergent dynamical phase is not closed by the noise. Similarly to the equilibrium topological phase, the dynamical transition here occurs when the minimal frequency on dBISs vanishes. For type-II transitions, the critical noise strength satisfies  $|w_{y,c} - w_{x,c}| = 2|h_z^*|$  and  $w_{x,c} + w_{y,c} = 2w_{z,c}$ , with  $|h_z^*|$  the minimal value of  $h_z$  at the topological charges where  $\mathbf{h}_{\text{so}} = 0$  (Appendix D). For  $|w_y - w_x| \geq 2|h_z^*|$ , the deformed

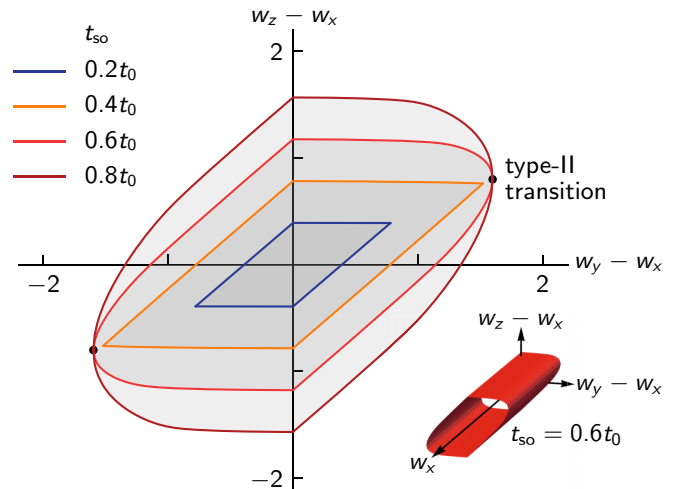


FIG. 4. Sweet spot region of QAH model. The lines represent the critical noise strength for different  $t_{\text{so}}$  values. The type-II transition point is indicated by the black points. In the sweet spot region (the shadow region), the dynamical topology survives at arbitrarily strong noise. The insert plot shows the full infinite sweet spot region extended along the  $w_x$  axis for  $t_{\text{so}} = 0.6t_0$  and with cross section being the same along  $w_x$  axis. Here we set  $m_z = 1.2t_0$ .

dBISs connect to topological charges [Figs. 2(g) and 2(h)], where oscillations always vanish and the emergent topology breaks down. For the type-I transition, the critical noise strength  $\mathbf{w}_c = (w_{x,c}, w_{y,c}, w_{z,c})$  is determined by

$$\min_{\mathbf{k} \in \text{dBISs}} \omega(\mathbf{k}; \mathbf{w}_c) = 0, \quad (12)$$

with  $\omega(\mathbf{k}) = 2\sqrt{\mathbf{h}_{\text{so}}^2(\mathbf{k}) - [\lambda_0(\mathbf{k})/4 - w_z]^2}$  and  $\lambda_0 = 2w_x h_x^2 / \mathbf{h}_{\text{so}}^2 + 2w_y h_y^2 / \mathbf{h}_{\text{so}}^2 + 2w_z$  (see Appendix D). Under the critical noise strength, certain dBIS momenta become exceptional, rendering a dynamical topological transition. Beyond the critical value the dynamical pattern becomes singular. Which type of transitions occurs first is parameter dependent.

A striking result is obtained from Eq. (12) that a *sweet spot* region is predicted as

$$\max_{\mathbf{k} \in \text{dBISs}} [(w_y - w_x)h_x^2 / \mathbf{h}_{\text{so}}^2 - 2|\mathbf{h}_{\text{so}}|] < w_z - w_x < \min_{\mathbf{k} \in \text{dBISs}} [(w_y - w_x)h_x^2 / \mathbf{h}_{\text{so}}^2 + 2|\mathbf{h}_{\text{so}}|], \quad (13)$$

in which the dynamical topology survives at arbitrarily strong noise. Here the upper and lower bounds of  $w_z - w_x$  are dependent only on  $w_y - w_x$  as the dBISs are fully determined by  $w_y - w_x$ . The type-II transition constrains  $|w_y - w_x| < 2|h_z^*|$ . The existence of the sweet spot region is an exotic feature of the dynamical topology, clearly beyond the equilibrium counterparts. In Fig. 4, we show the sweet spot region and the critical noise strength for the QAH model. The full sweet spot region is an infinite region extended along the  $w_x$  axis with the same cross section in the  $(w_z - w_x)$ - $(w_y - w_x)$  plot, which increases as the strength of spin-orbit coupling increases. The type-II transition can happen only for relatively large  $t_{\text{so}}$ . With a relatively large parameter range, the sweet spot region is observable in experiment [76].

## VII. CONCLUSION AND OUTLOOK

We have investigated the effects of dynamical noise on the quench-induced emergent dynamical topology, with universal results being predicted. We showed that the dynamical topology is robust against weak dynamical noise, and is protected by an effective bulk gap, i.e., the minimal oscillation frequency of the quench dynamics. Two novel types of dynamical transitions classified by distinct exceptional points or rings are predicted in the strong dynamical noise regime, with critical points being exactly obtained. Interestingly, we predicted a novel *sweet spot* region, in which the dynamical topology survives in arbitrarily strong noise, and the results are beyond the equilibrium counterparts. These universal results of the dynamical topology can be probed based on the recent experimental advances [57–60].

It is of great interest to generalize the study of noise effects on dynamical topology to higher-dimensional systems with higher bands and to other types of noise with colors, which will be left for future investigations. On the other hand, while having exceptional features, the emergent dynamical topological phases share similarities with the equilibrium counterparts, and the open questions can be further asked. In particular, as the nontrivial topology of an equilibrium phase brings about the broad nontrivial physics, e.g., the emergence of gapless boundary modes, exotic defect modes, topological responses under external field, etc., can the similar nontrivial physics in the dynamical version be obtained for the emergent dynamical topological phases? These issues are novel and deserve future studies.

## ACKNOWLEDGMENTS

This work was supported by National Natural Science Foundation of China (Grants No. 11825401, No. 11761161003, and No. 11921005), the National Key R&D Program of China (Project No. 2016YFA0301604), the Strategic Priority Research Program of Chinese Academy of Science (Grant No. XDB28000000), and the Open Project of Shenzhen Institute of Quantum Science and Engineering (Grant No. SIQSE202003).

## APPENDIX A: SPIN DYNAMICS ON THE dBISs

Here we prove that the spin polarization on dBISs evolves within the plane perpendicular to the SO axis  $\mathbf{h}_{\text{so}}$ . We notice that the spin component  $s_{\parallel}(\mathbf{k}, t) = \mathbf{s}_0^L(\mathbf{k}) \cdot \mathbf{s}(\mathbf{k}, t)$  satisfies  $\dot{s}_{\parallel}(\mathbf{k}, t) = -\lambda_0(\mathbf{k})s_{\parallel}(\mathbf{k}, t)$ . On the dBISs with  $\mathbf{s}_0^L(\mathbf{k}) \cdot \mathbf{s}(\mathbf{k}, 0) = 0$ , it is obvious that the component  $s_{\parallel}$  always vanishes, namely  $s_{\parallel}(\mathbf{k}, t) = 0$ . Thus the spin polarization evolves within the plane perpendicular to the component  $s_{\parallel}$ . On the other hand, for our initial state  $|\psi(\mathbf{k}, t=0)\rangle = |\uparrow\rangle$ , i.e.,  $\mathbf{s}(\mathbf{k}, 0) = (0, 0, 1)$ ,  $\mathbf{s}_0^L$  on dBISs generally takes the form  $\mathbf{s}_0^L = (\alpha, \beta, 0)$ . Substituting this into Eq. (6), we have  $\mathbf{s}_0^L \sim (h_x, h_y, 0)$  on the dBISs and  $s_{\parallel} = h_x s_x + h_y s_y$ , which is parallel to the SO axis  $\mathbf{h}_{\text{so}}$  in the Bloch sphere. Therefore, on the dBISs the spin polarization evolves within the plane perpendicular to the SO axis  $\mathbf{h}_{\text{so}}$ , which is valid both for weak noise and strong noise.

With  $\mathbf{s}_0^L \sim (h_x, h_y, 0)$  on the dBISs, we can solve from Eq. (6) the explicit expression for dBISs  $h_z =$

$(w_y - w_x)h_x h_y / \mathbf{h}_{\text{so}}^2$  and the eigenvalue  $\lambda_0 = 2w_x h_y^2 / \mathbf{h}_{\text{so}}^2 + 2w_y h_x^2 / \mathbf{h}_{\text{so}}^2 + 2w_z$ . Together with the relation  $\mathbf{s}_0^L \cdot \mathbf{s}_0^R = 1$ , we also obtain the  $x, y$  components of the right eigenvector  $\mathbf{s}_0^R$  on the dBISs as  $(s_{0,x}^R, s_{0,y}^R)_{\text{dBIS}} \sim (h_x(1 - \eta), h_y(1 + \eta))$ , giving the explicit form of dynamical field  $\mathbf{g}$  in the main text. It is obvious that the noise cannot fully flip the SO field, namely  $\mathbf{g} \not\propto -\mathbf{h}_{\text{so}}$ ; otherwise we must have  $1 - \eta = 1 + \eta < 0$ , which is impossible.

## APPENDIX B: PROOF FOR THE ROBUSTNESS OF DYNAMICAL TOPOLOGY

Here we first show that as the noise increases from zero to the weak regime, no topological charge passes through the deformed dBISs. The proof is given as follows. For the momenta of topological charges with  $\mathbf{h}_{\text{so}}(\mathbf{k}) = 0$ , the spin dynamics with initial state  $\mathbf{s}(t=0) = (0, 0, 1)$  is given by  $s_x(t) = s_y(t) = 0$  and  $s_z(t) = e^{-2(w_x + w_y)t}$ , and the corresponding dynamical spin polarization reads  $\tilde{\mathbf{s}}(t) = (0, 0, 1)$ . If we gradually increase the strength of noise from zero to some weak noise, the dBISs will be deformed from the BISs to the final ones but no topological charge passes through them; otherwise there will be momenta on the dBISs with  $\tilde{\mathbf{s}}(\mathbf{k}) \neq 0$  for the intermediate weak noise, which is impossible. Thus no topological charge passes through the deformed dBISs. Consequently, the topological charges enclosed by the dBISs remain unchanged; so does the winding of the SO field  $\mathbf{h}_{\text{so}}$  on the dBISs in the weak-noise regime.

We now prove the robustness of the dynamical topology by showing that the winding of the dynamical field  $\mathbf{g}$  on the dBISs is equivalent to that of the SO field  $\mathbf{h}_{\text{so}}$ . We can introduce two auxiliary gapped Hamiltonians defined on the one-dimensional dBISs,  $H_1(\mathbf{k}) = g_x(\mathbf{k})\sigma_x + g_y(\mathbf{k})\sigma_y$  and  $H_2(\mathbf{k}) = h_x(\mathbf{k})\sigma_x + h_y(\mathbf{k})\sigma_y$  with  $\mathbf{k} \in \text{dBIS}$ , of which the winding number characterizes the winding of dynamical field  $\mathbf{g}$  and SO field  $\mathbf{h}_{\text{so}}$ , respectively. Without changing the winding number, we can choose  $(g_x, g_y)$  as  $(h_x(1 - \eta), h_y(1 + \eta))$  while ignoring the normalization factor. Consider the continuous deformation  $H_q = qH_1 + (1 - q)H_2$  with  $0 \leq q \leq 1$ ; we have  $H_q^2 = (1 - q\eta)^2 h_x^2 + (1 + q\eta)^2 h_y^2$ . Since  $1 - q\eta$  and  $1 + q\eta$  cannot be zero simultaneously, we must have  $H_q^2 > 0$  for  $h_{x,y} \neq 0$ . For the case with  $h_x = 0$  (or  $h_y = 0$ ), we have  $\mathbf{g} \sim (0, h_y)$  [or  $\mathbf{g} \sim (h_x, 0)$ ], from which it is obvious that  $H_q^2 > 0$ . Therefore,  $H_q$  is gapped for  $0 \leq q \leq 1$ , indicating that  $H_1$  and  $H_2$  are topologically equivalent. This proves that for the weak noise with damped oscillation for spin dynamics on dBISs, the winding of dynamical field  $\mathbf{g}(\mathbf{k})$  is topologically equivalent to that of the SO field and remains invariant.

## APPENDIX C: EXCEPTIONAL POINT OR RING OF THE LIOUVILLIAN SUPEROPERATOR

The properties of the eigenvalues of Liouvillian superoperator  $\mathcal{L}$  are determined by the corresponding discriminant  $\Delta$  (see main text). For  $\Delta > 0$ , we have one real eigenvalue and a conjugate pair of complex eigenvalues. The eigenvalues are all real with at least two equal if  $\Delta = 0$ . For  $\Delta < 0$ , the three real eigenvalues are distinct from each other. These three cases correspond to positive  $\omega$ ,  $\omega = 0$  and purely imaginary  $\omega$ , respectively.

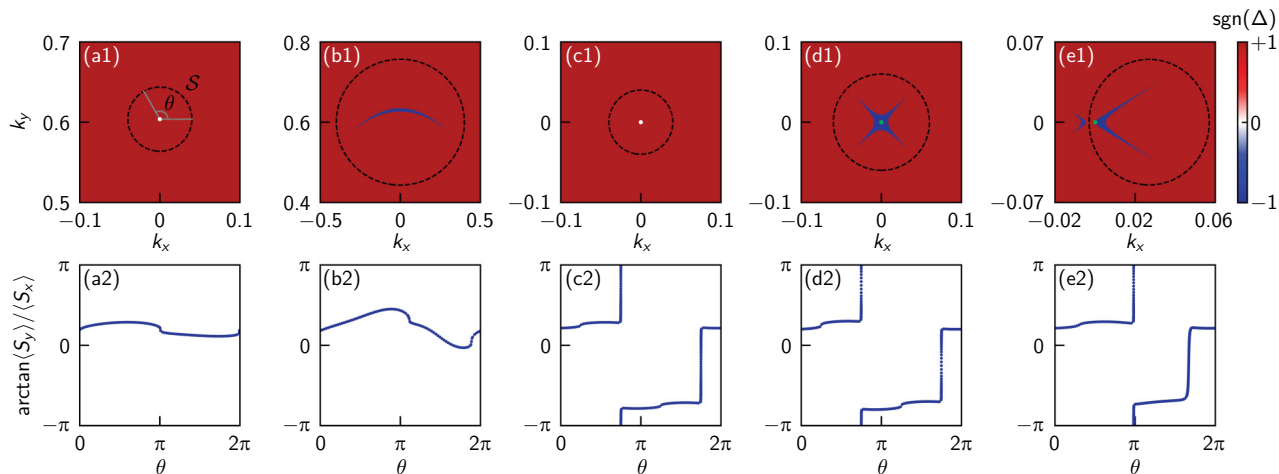


FIG. 5. Possible configurations of exceptional point or ring of Liouvillian superoperator. In the upper panel, we plot the signs of discriminant  $\Delta$ . The isolated momentum with  $\Delta = 0$  (white dot) is the exceptional point, and the boundary of the blue cluster also has  $\Delta = 0$  and is the exceptional ring. The loop  $\mathcal{S}$  (black dashed line) is chosen as an ellipse with  $(x_0 + r_x \cos \theta, y_0 + r_y \sin \theta)$ . The lower panel shows the corresponding windings of the vector  $(\langle S_x \rangle, \langle S_y \rangle)$  as the eccentric angle  $\theta$  of the elliptical loop  $\mathcal{S}$  varies from 0 to  $2\pi$ . (a) Isolated type-I exceptional point at  $\mathbf{k} \approx (0, 0.60375)$ . (b) Type-I exceptional ring. (c) Isolated type-II exceptional point at the charge momentum  $\mathbf{k} = (0, 0)$ . (d) Type-II exceptional ring enclosing the charge momentum (green dot). (e) Type-II exceptional ring containing the charge momentum; i.e., the charge momentum is on the exceptional ring. The type-I exceptional point or ring [(a), (b)] is characterized by a trivial winding number, while the type-II exceptional point or ring [(c)–(e)] has a nonzero winding number equal to the charge value  $+1$ . Here the model is  $H(\mathbf{k}) = \mathbf{h}(\mathbf{k}) \cdot \boldsymbol{\sigma}$  with  $h_x = t_{so} \sin k_x$ ,  $h_y = t_{so} \sin k_y$ ,  $h_z = m_z - t_0 \cos k_x - t_0 \cos k_y$  for (a)–(d) and  $h_z = m_z - t_0 \cos(k_x + 0.1) - t_0 \cos k_y$  for (e). We set  $m_z = 1.2t_0$  and  $t_{so} = 2t_0$ . The noise strength for (a)–(e) is  $(w_x, w_y, w_z) = (0.5, 0, 2.451265)t_0, (0.5, 0, 2.6)t_0, (1.6, 0, 0.8)t_0, (1.61, 0, 0.8)t_0$ , and  $(2|0.2 - \cos 0.1|, 0, 0.7)t_0$ , respectively.

Suppose that the discriminant  $\Delta$  is zero for certain momentum, i.e.,  $\omega = 0$ , leading to a multiple eigenvalue  $\lambda$  with algebraic multiplicity greater than 1. The dimension of the eigenspace associated with  $\lambda$  is determined by the nullity of

$\mathcal{L} + \lambda I$ . If the nullity is smaller than the algebraic multiplicity, the corresponding momentum is exceptional for the Liouvillian superoperator. Consider the momentum with  $h_i \neq 0$  for  $i = x, y, z$ ; we have for the multiple eigenvalue  $\lambda$

$$\mathcal{L} + \lambda I \xrightarrow[\text{elimination}]{\text{Gaussian}} \begin{bmatrix} 2h_z & \lambda - 2(w_x + w_z) & -2h_x \\ 0 & -2h_z - \frac{[\lambda - 2(w_x + w_z)][\lambda - 2(w_y + w_z)]}{2h_z} & 2h_y + \frac{h_x[\lambda - 2(w_y + w_z)]}{h_z} \\ 0 & 2h_x + \frac{h_y[\lambda - 2(w_x + w_z)]}{h_z} & \lambda - 2(w_x + w_y) - \frac{2h_x h_y}{h_z} \end{bmatrix}. \quad (C1)$$

Since the last two rows cannot simultaneously be zero for the considered momentum, the rank of  $\mathcal{L} + \lambda I$  is greater than 1. Hence the nullity is smaller than 2 and is smaller than the algebraic multiplicity of  $\lambda$ , manifesting that the considered momentum with a multiple eigenvalue is exceptional. Similar analysis for other momenta with possible  $\mathbf{h}(\mathbf{k})$  suggests that when there exists a multiple eigenvalue for the eigenequation  $\det(\mathcal{L} + \lambda I) = 0$ , i.e.,  $\Delta = 0$  and  $\omega = 0$ , the corresponding momentum is exceptional for the Liouvillian superoperator.

The possible configurations of exceptional momenta are shown in the upper panel of Fig. 5. For the Liouvillian superoperator, both the isolated exceptional points [Figs. 5(a1) and 5(c1)] and the exceptional rings [Figs. 5(b1), 5(d1), and 5(e1)] are possible. The isolated exceptional point of the Liouvillian superoperator just emerges under certain noise strength without the creation of a pair of opposite valued exceptional points, and it becomes an exceptional ring when the noise strength further increases.

To characterize the exceptional point or ring, the winding number  $N_E$  has been introduced in the main text. Denote  $\mathbf{s}_+^R = (\alpha, \beta, \gamma)^T$  being the right eigenvector of  $\mathcal{L}$  with eigenvalue  $-\lambda_+ = -(\lambda_1 + i\omega)$ ; we have  $\langle S_x \rangle = -i\beta^* \gamma + i\gamma^* \beta$  and  $\langle S_y \rangle = i\alpha^* \gamma - i\gamma^* \alpha$ . Note that we can always find a gauge such that  $\gamma$  is real. On the exceptional point or ring, it is obvious that the right eigenvector  $\mathbf{s}_+^R$  is real and the vector  $(\langle S_x \rangle, \langle S_y \rangle)$  vanishes. On the other hand, we always have  $\gamma = 0$  and  $(\langle S_x \rangle, \langle S_y \rangle) = 0$  for the charge momenta with  $\mathbf{h}_{so} = 0$ . In this sense, both the exceptional point or ring and the charge momentum are singular points. For other momenta not being either the exceptional point or ring, on one hand, or the charge momenta, on the other, we have nonzero oscillation frequency; i.e., the eigenvalue is a complex number. Hence  $\mathbf{s}_+^R$  cannot be real and  $\gamma \neq 0$ . For this, the vector  $(\langle S_x \rangle, \langle S_y \rangle)$  is always nonzero on these momenta. Based on these facts, the winding number  $N_E$  of  $(\langle S_x \rangle, \langle S_y \rangle)$  on a loop  $\mathcal{S}$  enclosing the exceptional point or ring but not enclosing other singular

points is well defined and can be used to characterize the exceptional point or ring.

**1. Classification of exceptional points or rings**

According to the relation with the charge momentum and the winding number  $N_E$ , the exceptional points or rings of the Liouvillian superoperator can be generally categorized into two types:

(i) Type-I exceptional point or ring: Isolated exceptional point not at the charge momentum or exceptional ring not enclosing nor containing the charge momentum, for which  $N_E$  is trivial; see Figs. 5(a) and 5(b).

(ii) Type-II exceptional point or ring: Isolated exceptional point at the charge momentum or exceptional ring enclosing or containing the charge momentum, for which  $N_E$  equals the charge value; see Figs. 5(c)–5(e).

In the following, we utilize the general properties of winding number  $N_E$  to prove this classification.

*a. Type-I exceptional point or ring*

We start with the isolated type-I exceptional point not at the charge momentum, near which there is no other singular point; see Fig. 5(a1). To prove its triviality, we notice that the isolated exceptional point of the Liouvillian superoperator just emerges under certain noise strength. For an arbitrary isolated type-I exceptional point, we can fix a loop  $\mathcal{S}$  enclosing it and gradually decrease the noise strength such that this isolated exceptional point disappears. During this process, there is no singular point passing through the loop  $\mathcal{S}$  and the oscillation frequency on  $\mathcal{S}$  is always nonzero, indicating that the vector  $(\langle S_x \rangle, \langle S_y \rangle)$  does not vanish. Thus the winding of  $(\langle S_x \rangle, \langle S_y \rangle)$  for the isolated type-I exceptional point is topologically equivalent to the one without any singular point enclosed by  $\mathcal{S}$ . With this, we conclude that the isolated type-I exceptional point is characterized by a trivial winding number  $N_E$ ; see Fig. 5(a2).

We next consider the type-I exceptional ring, which does not enclose or contain the charge momenta [Fig. 5(b1)]. Generally, the type-I exceptional ring will become smaller and smaller as we decrease the noise strength and finally disappears. For its winding  $N_E$ , we can either fix a large loop  $\mathcal{S}$  or deform  $\mathcal{S}$  to follow the exceptional ring during the process with decreased noise strength. The loop does not cross any singular point. Then the vector  $(\langle S_x \rangle, \langle S_y \rangle)$  on  $\mathcal{S}$  is always nonzero and its winding number remains unchanged. On the other hand, when the exceptional ring enclosed by  $\mathcal{S}$  disappears, the winding of  $(\langle S_x \rangle, \langle S_y \rangle)$  is obviously trivial, as there is no singular point enclosed by  $\mathcal{S}$ . Hence the type-I exceptional ring is also characterized by a trivial winding number  $N_E$ , as illustrated in Fig. 5(b2).

*b. Type-II exceptional point or ring*

The type-II exceptional point refers to the isolated exceptional point located at the charge momentum; see Fig. 5(c1). Similar to the isolated type-I exceptional point, we can fix a loop  $\mathcal{S}$  enclosing the type-II exceptional point and gradually decrease the noise strength such that this isolated exceptional point disappears. During this process, the winding number  $N_E$

on  $\mathcal{S}$  remains unchanged and is topologically equivalent to the one without noise. The difference is that the charge momentum is also a singular point for the vector  $(\langle S_x \rangle, \langle S_y \rangle)$ , which is enclosed by the loop  $\mathcal{S}$ . Hence the winding number of the type-II exceptional point is the same as the one of topological charge without noise, near which the right eigenvector  $s_+^R$  is given by

$$s_+^R = \frac{1}{\mathcal{N}} \left( \frac{i\omega h_y/2 - h_x h_z}{\omega^2/4 - h_z^2}, -\frac{i\omega h_x/2 + h_y h_z}{\omega^2/4 - h_z^2}, 1 \right)^T \quad (C2)$$

with eigenvalue  $-i\omega$  and  $\omega = 2|\mathbf{h}|$ . We obtain

$$(\langle S_x \rangle, \langle S_y \rangle) = \frac{\omega}{\mathcal{N}^2(\omega^2/4 - h_z^2)} (h_x, h_y), \quad (C3)$$

where  $\omega, \omega^2/4 - h_z^2$  are always positive and for which the winding number is equal to the charge value, i.e., the winding number of  $(h_x, h_y)$ . With this, the isolated type-II exceptional point is characterized by a nontrivial winding number  $N_E$  with the charge value; see Fig. 5(c2).

For the type-II exceptional ring, which encloses the charge momentum [Fig. 5(d1)] or contains the charge momentum [Fig. 5(e1)], we can use the similar argument of type-I exceptional rings to obtain its winding number. That is, we can either fix a large loop  $\mathcal{S}$  or deform  $\mathcal{S}$  to follow the exceptional ring during the process with decreased noise strength, provided that the loop does not cross any singular point. Then we calculate the winding number of  $(\langle S_x \rangle, \langle S_y \rangle)$  on  $\mathcal{S}$  when the noise strength decreases to zero, which is topologically equivalent to the one of type-II exceptional ring. Note that the loop enclosing the type-II exceptional ring also encloses the charge momentum, which is always a singular point for the vector  $(\langle S_x \rangle, \langle S_y \rangle)$ . When the noise strength decreases to zero and the type-II exceptional ring disappears, the loop  $\mathcal{S}$  should still enclose the charge momentum. Hence the type-II exceptional ring is characterized by a nontrivial winding number  $N_E$  equal to the charge value; see Figs. 5(d2) and 5(e2).

**2. Classification of dynamical transitions**

We now show the classification of dynamical transitions by the exceptional points or rings of the Liouvillian superoperator. For type-I dynamical transitions, the deformation of dBISs is relatively small, but the minimal oscillation frequency over the dBISs vanishes for the critical noise strength  $w_c$ . Under this critical noise strength, certain momenta of dBISs with vanishing minimal frequency become exceptional, which are either isolated type-I exceptional points or belong to type-I exceptional rings. Therefore, the type-I dynamical transition can be understood as the isolated type-I exceptional point emerges on the dBISs [Fig. 6(a)] or the type-I exceptional ring touches the dBISs [Fig. 6(b)]. As shown above, the type-I exceptional points or rings are characterized by a trivial winding number  $N_E$ .

For the type-II dynamical transition, the dBISs are deformed dramatically and even connect to the topological charges for the critical noise strength  $w_c$ , under which the charge momentum has  $\omega = 0$ . Although both types of dynamical transition indicate that the minimal oscillation frequency over the dBISs vanishes for the critical noise strength, the type-II transition indeed differs from the type-I transition.



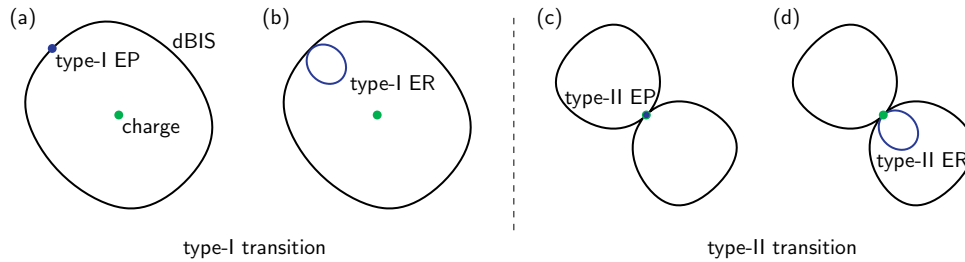


FIG. 6. Schematic illustration of two types of dynamical transition classified by the exceptional points or rings. (a), (b) The type-I transition. The isolated type-I exceptional point (blue dot) emerges on the dBISs (black line) (a), or the type-I exceptional ring (blue line) touches the dBISs (b), rendering the type-I dynamical transition. (c), (d) The type-II transition. The dBIS is deformed to connect to the charge momentum (green dot), which is exceptional. The charge momentum is either an isolated type-II exceptional point (c) or belongs to a type-II exceptional ring containing the charge momentum (d). Here EP (ER) denotes the exceptional point (ring).

Under the type-II critical noise strength  $w_c$ , the charge momentum is the only momentum on dBISs being exceptional. According to the above classification of exceptional points or rings, the charge momentum is either an isolated type-II exceptional point [Fig. 6(c)] or belongs to a type-II exceptional ring containing the charge momentum [Fig. 6(d)], which are characterized by a nonzero winding number  $N_E$  equal to the charge value. Thus the type-II dynamical transition is driven by the type-II exceptional point or ring, while the type-I transition is related to the type-I exceptional point or ring. The distinct exceptional point or ring shows the fundamental difference between the type-I and type-II dynamical transitions.

#### APPENDIX D: DERIVATION OF THE CRITICAL NOISE STRENGTH

To obtain the critical noise strength for type-I transitions, we need to solve the oscillation frequency on dBISs from the eigenequation  $\det(\mathcal{L} + \lambda I) = 0$ , namely  $(\lambda - \lambda_0)[\lambda^2 + (b + \lambda_0)\lambda + \lambda_0^2 + b\lambda_0 + c] = 0$ . We have  $\lambda_{\pm}^2 + (b + \lambda_0)\lambda_{\pm} + \lambda_0^2 + b\lambda_0 + c = 0$ , and the oscillation frequency on dBISs is given by  $\omega = 2\sqrt{\mathbf{h}_{s_0}^2 - [\lambda_0/4 - w_z]^2}$ . The vanishing minimal oscillation frequency over dBISs gives the type-I critical noise strength in the main text.

For type-II dynamical transitions, the dBISs are deformed to connect to the topological charges. To see this, we consider

a continuous path  $P$  with fixed  $h_x h_y / (h_x^2 + h_y^2)$  connecting the corresponding momentum on BISs with  $h_z = 0$  to the topological charge with  $\mathbf{h} = (0, 0, h_z^*)$ . As  $|w_y - w_x|$  increases, the dBIS momentum with  $|h_z| = [|h_x h_y / (h_x^2 + h_y^2)| |w_y - w_x|]$  will move along the path  $P$ . Due to  $h_x^2 + h_y^2 \geq 2|h_x h_y|$ , the dBIS momentum varying most rapidly belongs to the path  $P$  with  $|h_x h_y / (h_x^2 + h_y^2)| = 1/2$ , namely  $|h_x| = |h_y|$ , for which we have  $|h_z| = |w_y - w_x|/2$ . When  $|w_y - w_x|$  increases to  $2|h_z^*|$ , we have  $h_z = h_z^*$  on the dBIS momentum, indicating that the dBISs connect to the topological charge.

We can also examine the spin dynamics of topological charge. It is easy to find that the corresponding oscillation frequency is nonzero for  $|w_y - w_x| < 2|h_z^*|$ , and the topological charge cannot belong to the dBISs due to  $s_0^L \cdot s(0) \neq 0$ . However, the oscillation frequency vanishes for  $|w_y - w_x| \geq 2|h_z^*|$  and we have the eigenvector  $s_+^L \sim (\alpha, \beta, 0)$  for real  $\lambda_+$  satisfying the dBIS condition  $s_+^L \cdot s(0) = 0$ , from which the deformed dBISs indeed connect to the topological charge.

The above analysis shows the type-II critical noise strength  $|w_{y,c} - w_{x,c}| = 2|h_z^*|$ . On the other hand, the type-I transition should not happen before the dBISs connect to topological charges; otherwise there is no type-II transition. This means that as the dBIS momenta with  $|h_x| = |h_y|$  approach the topological charges, i.e.,  $\mathbf{h}_{s_0} \rightarrow 0$ , the corresponding frequencies should always be nonzero, leading to  $w_{x,c} + w_{y,c} = 2w_{z,c}$ . With this condition, the charge momentum is the only point on dBISs being exceptional when the type-II transition occurs.

[1] K. v. Klitzing, G. Dorda, and M. Pepper, New Method for High-Accuracy Determination of the Fine-Structure Constant Based on Quantized Hall Resistance, *Phys. Rev. Lett.* **45**, 494 (1980).  
 [2] D. J. Thouless, M. Kohmoto, M. P. Nightingale, and M. den Nijs, Quantized Hall Conductance in a Two-Dimensional Periodic Potential, *Phys. Rev. Lett.* **49**, 405 (1982).  
 [3] F. D. M. Haldane, Model for a Quantum Hall Effect without Landau Levels: Condensed-Matter Realization of the ‘‘Parity Anomaly’’, *Phys. Rev. Lett.* **61**, 2015 (1988).  
 [4] M. Z. Hasan and C. L. Kane, *Colloquium: Topological insulators*, *Rev. Mod. Phys.* **82**, 3045 (2010).  
 [5] X.-L. Qi and S.-C. Zhang, Topological insulators and superconductors, *Rev. Mod. Phys.* **83**, 1057 (2011).  
 [6] C.-K. Chiu, J. C. Y. Teo, A. P. Schnyder, and S. Ryu, Classification of topological quantum matter with symmetries, *Rev. Mod. Phys.* **88**, 035005 (2016).  
 [7] C. L. Kane and E. J. Mele, Quantum Spin Hall Effect in Graphene, *Phys. Rev. Lett.* **95**, 226801 (2005).  
 [8] B. A. Bernevig, T. L. Hughes, and S.-C. Zhang, Quantum spin Hall effect and topological phase transition in HgTe quantum wells, *Science* **314**, 1757 (2006).  
 [9] M. König, S. Wiedmann, C. Brüne, A. Roth, H. Buhmann, L. W. Molenkamp, X.-L. Qi, and S.-C. Zhang, Quantum spin Hall insulator state in HgTe quantum wells, *Science* **318**, 766 (2007).  
 [10] C.-Z. Chang, J. Zhang, X. Feng, J. Shen, Z. Zhang, M. Guo, K. Li, Y. Ou, P. Wei, L.-L. Wang, Z.-Q. Ji, Y. Feng, S. Ji, X. Chen,

- J. Jia, X. Dai, Z. Fang, S.-C. Zhang, K. He, Y. Wang, L. Lu, X.-C. Ma, and Q.-K. Xue, Experimental observation of the quantum anomalous Hall effect in a magnetic topological insulator, *Science* **340**, 167 (2013).
- [11] F. D. M. Haldane and S. Raghu, Possible Realization of Directional Optical Waveguides in Photonic Crystals with Broken Time-Reversal Symmetry, *Phys. Rev. Lett.* **100**, 013904 (2008).
- [12] M. C. Rechtsman, J. M. Zeuner, Y. Plotnik, Y. Lumer, D. Podolsky, F. Dreisow, S. Nolte, M. Segev, and A. Szameit, Photonic Floquet topological insulators, *Nature (London)* **496**, 196 (2013).
- [13] A. B. Khanikaev, S. Hossein Mousavi, W. K. Tse, M. Kargarian, A. H. MacDonald, and G. Shvets, Photonic topological insulators, *Nat. Mater.* **12**, 233 (2013).
- [14] T. Ozawa, H. M. Price, A. Amo, N. Goldman, M. Hafezi, L. Lu, M. C. Rechtsman, D. Schuster, J. Simon, O. Zilberberg, and I. Carusotto, Topological photonics, *Rev. Mod. Phys.* **91**, 015006 (2019).
- [15] X.-J. Liu, Z.-X. Liu, and M. Cheng, Manipulating Topological Edge Spins in a One-Dimensional Optical Lattice, *Phys. Rev. Lett.* **110**, 076401 (2013).
- [16] X.-J. Liu, K. T. Law, and T. K. Ng, Realization of 2D Spin-Orbit Interaction and Exotic Topological Orders in Cold Atoms, *Phys. Rev. Lett.* **112**, 086401 (2014).
- [17] M. Aidelsburger, M. Atala, M. Lohse, J. T. Barreiro, B. Paredes, and I. Bloch, Realization of the Hofstadter Hamiltonian with Ultracold Atoms in Optical Lattices, *Phys. Rev. Lett.* **111**, 185301 (2013).
- [18] H. Miyake, G. A. Siviloglou, C. J. Kennedy, W. C. Burton, and W. Ketterle, Realizing the Harper Hamiltonian with Laser-Assisted Tunneling in Optical Lattices, *Phys. Rev. Lett.* **111**, 185302 (2013).
- [19] G. Jotzu, M. Messer, R. Desbuquois, M. Lebrat, T. Uehlinger, D. Greif, and T. Esslinger, Experimental realization of the topological Haldane model with ultracold fermions, *Nature (London)* **515**, 237 (2014).
- [20] M. Aidelsburger, M. Lohse, C. Schweizer, M. Atala, J. Barreiro, S. Nascimbène, N. Cooper, I. Bloch, and N. Goldman, Measuring the Chern number of Hofstadter bands with ultracold bosonic atoms, *Nat. Phys.* **11**, 162 (2015).
- [21] Z. Wu, L. Zhang, W. Sun, X.-T. Xu, B.-Z. Wang, S.-C. Ji, Y. Deng, S. Chen, X.-J. Liu, and J.-W. Pan, Realization of two-dimensional spin-orbit coupling for Bose-Einstein condensates, *Science* **354**, 83 (2016).
- [22] A. P. Schnyder, S. Ryu, A. Furusaki, and A. W. W. Ludwig, Classification of topological insulators and superconductors in three spatial dimensions, *Phys. Rev. B* **78**, 195125 (2008).
- [23] A. Kitaev, Periodic table for topological insulators and superconductors, *AIP Conf. Proc.* **1134**, 22 (2009).
- [24] S. Ryu, A. P. Schnyder, A. Furusaki, and A. W. W. Ludwig, Topological insulators and superconductors: Tenfold way and dimensional hierarchy, *New J. Phys.* **12**, 065010 (2010).
- [25] B. Yan and S.-C. Zhang, Topological materials, *Rep. Prog. Phys.* **75**, 096501 (2012).
- [26] B. Yan and C. Felser, Topological materials: Weyl semimetals, *Annu. Rev. Condens. Matter Phys.* **8**, 337 (2017).
- [27] T. Zhang, Y. Jiang, Z. Song, H. Huang, Y. He, Z. Fang, H. Weng, and C. Fang, Catalogue of topological electronic materials, *Nature (London)* **566**, 475 (2019).
- [28] M. G. Vergniory, L. Elcoro, C. Felser, N. Regnault, B. A. Bernevig, and Z. Wang, A complete catalog of high-quality topological materials, *Nature (London)* **566**, 480 (2019).
- [29] F. Tang, H. C. Po, A. Vishwanath, and X. Wan, Comprehensive search for topological materials using symmetry indicators, *Nature (London)* **566**, 486 (2019).
- [30] M. D. Caio, N. R. Cooper, and M. J. Bhaseen, Quantum Quenches in Chern Insulators, *Phys. Rev. Lett.* **115**, 236403 (2015).
- [31] Y. Hu, P. Zoller, and J. C. Budich, Dynamical Buildup of a Quantized Hall Response from Nontopological States, *Phys. Rev. Lett.* **117**, 126803 (2016).
- [32] C. Wang, P. Zhang, X. Chen, J. Yu, and H. Zhai, Scheme to Measure the Topological Number of a Chern Insulator from Quench Dynamics, *Phys. Rev. Lett.* **118**, 185701 (2017).
- [33] N. Fläschner, D. Vogel, M. Tarnowski, B. S. Rem, D. S. Lühmann, M. Heyl, J. C. Budich, L. Mathey, K. Sengstock, and C. Weitenberg, Observation of dynamical vortices after quenches in a system with topology, *Nat. Phys.* **14**, 265 (2018).
- [34] B. Song, L. Zhang, C. He, T. F. J. Poon, E. Hagiyevev, S. Zhang, X.-J. Liu, and G.-B. Jo, Observation of symmetry-protected topological band with ultracold fermions, *Sci. Adv.* **4**, aao4748 (2018).
- [35] M. McGinley and N. R. Cooper, Classification of topological insulators and superconductors out of equilibrium, *Phys. Rev. B* **99**, 075148 (2019).
- [36] H. Cai, J. Liu, J. Wu, Y. He, S.-Y. Zhu, J.-X. Zhang, and D.-W. Wang, Experimental Observation of Momentum-Space Chiral Edge Currents in Room-Temperature Atoms, *Phys. Rev. Lett.* **122**, 023601 (2019).
- [37] Y.-H. Lu, B.-Z. Wang, and X.-J. Liu, Ideal Weyl semimetal with 3D spin-orbit coupled ultracold quantum gas, *Sci. Bull.* **65**, 2080 (2020).
- [38] X. Qiu, T.-S. Deng, Y. Hu, P. Xue, and W. Yi, Fixed points and dynamic topological phenomena in a parity-time-symmetric quantum quench, *iScience* **20**, 392 (2019).
- [39] D. Xie, T.-S. Deng, T. Xiao, W. Gou, T. Chen, W. Yi, and B. Yan, Topological Quantum Walks in Momentum Space with a Bose-Einstein Condensate, *Phys. Rev. Lett.* **124**, 050502 (2020).
- [40] H. Hu and E. Zhao, Topological Invariants for Quantum Quench Dynamics from Unitary Evolution, *Phys. Rev. Lett.* **124**, 160402 (2020).
- [41] X. Chen, C. Wang, and J. Yu, Linking invariant for the quench dynamics of a two-dimensional two-band Chern insulator, *Phys. Rev. A* **101**, 032104 (2020).
- [42] L. Zhang, L. Zhang, S. Niu, and X.-J. Liu, Dynamical classification of topological quantum phases, *Sci. Bull.* **63**, 1385 (2018).
- [43] L. Zhang, L. Zhang, and X.-J. Liu, Dynamical detection of topological charges, *Phys. Rev. A* **99**, 053606 (2019).
- [44] L. Zhang, L. Zhang, and X.-J. Liu, Characterizing topological phases by quantum quenches: A general theory, *Phys. Rev. A* **100**, 063624 (2019).
- [45] L. Zhang, L. Zhang, Y. Hu, N. Sen, and X.-J. Liu, Emergent topology and symmetry-breaking order in correlated quench dynamics, [arXiv:1903.09144](https://arxiv.org/abs/1903.09144).
- [46] X.-L. Yu, W. Ji, L. Zhang, Y. Wang, J. Wu, X.-J. Liu, Quantum dynamical characterization and simulation of topological phases with high-order band inversion surfaces, [arXiv:2004.14930](https://arxiv.org/abs/2004.14930).

- [47] L. Zhang, L. Zhang, and X.-J. Liu, Unified Theory to Characterize Floquet Topological Phases by Quench Dynamics, *Phys. Rev. Lett.* **125**, 183001 (2020).
- [48] W. Jia, L. Zhang, L. Zhang, and X.-J. Liu, Dynamically characterizing topological phases by high-order topological charges, [arXiv:2012.13494](https://arxiv.org/abs/2012.13494).
- [49] L. Zhou and J. Gong, Non-Hermitian Floquet topological phases with arbitrarily many real-quasienergy edge states, *Phys. Rev. B* **98**, 205417 (2018).
- [50] B. Zhu, Y. Ke, H. Zhong, and C. Lee, Dynamic winding number for exploring band topology, *Phys. Rev. Res.* **2**, 023043 (2020).
- [51] L. Li, W. Zhu, and J. Gong, Direct dynamical characterization of higher-order topological insulators with nested band inversion surfaces, [arXiv:2007.05759](https://arxiv.org/abs/2007.05759).
- [52] J. Ye and F. Li, Emergent topology under slow nonadiabatic quantum dynamics, *Phys. Rev. A* **102**, 042209 (2020).
- [53] D. Yu, B. Peng, X. Chen, X.-J. Liu, and L. Yuan, Topological holographic quench dynamics in a synthetic dimension, [arXiv:2101.08606](https://arxiv.org/abs/2101.08606).
- [54] W. Sun, C.-R. Yi, B.-Z. Wang, W.-W. Zhang, B. C. Sanders, X.-T. Xu, Z.-Y. Wang, J. Schmiedmayer, Y. Deng, X.-J. Liu, S. Chen, and J.-W. Pan, Uncover Topology by Quantum Quench Dynamics, *Phys. Rev. Lett.* **121**, 250403 (2018).
- [55] C.-R. Yi, L. Zhang, L. Zhang, R.-H. Jiao, X.-C. Cheng, Z.-Y. Wang, X.-T. Xu, W. Sun, X.-J. Liu, S. Chen, and J.-W. Pan, Observing Topological Charges and Dynamical Bulk-Surface Correspondence with Ultracold Atoms, *Phys. Rev. Lett.* **123**, 190603 (2019).
- [56] B. Song, C. He, S. Niu, L. Zhang, Z. Ren, X.-J. Liu, and G.-B. Jo, Observation of nodal-line semimetal with ultracold fermions in an optical lattice, *Nat. Phys.* **15**, 911 (2019).
- [57] Y. Wang, W. Ji, Z. Chai, Y. Guo, M. Wang, X. Ye, P. Yu, L. Zhang, X. Qin, P. Wang, F. Shi, X. Rong, D. Lu, X.-J. Liu, and J. Du, Experimental observation of dynamical bulk-surface correspondence in momentum space for topological phases, *Phys. Rev. A* **100**, 052328 (2019).
- [58] W. Ji, L. Zhang, M. Wang, L. Zhang, Y. Guo, Z. Chai, X. Rong, F. Shi, X.-J. Liu, Y. Wang, and J. Du, Quantum Simulation for Three-Dimensional Chiral Topological Insulator, *Phys. Rev. Lett.* **125**, 020504 (2020).
- [59] T. Xin, Y. Li, Y.-A. Fan, X. Zhu, Y. Zhang, X. Nie, J. Li, Q. Liu, and D. Lu, Quantum Phases of Three-Dimensional Chiral Topological Insulators on a Spin Quantum Simulator, *Phys. Rev. Lett.* **125**, 090502 (2020).
- [60] J. Niu, T. Yan, Y. Zhou, Z. Tao, X. Li, W. Liu, L. Zhang, S. Liu, Z. Yan, Y. Chen, and D. Yu, Simulation of higher-order topological phases and related topological phase transitions in a superconducting qubit, [arXiv:2001.03933](https://arxiv.org/abs/2001.03933).
- [61] D. N. Sheng, Z. Y. Weng, L. Sheng, and F. D. M. Haldane, Quantum Spin-Hall Effect and Topologically Invariant Chern Numbers, *Phys. Rev. Lett.* **97**, 036808 (2006).
- [62] M. Onoda, Y. Avishai, and N. Nagaosa, Localization in a Quantum Spin Hall System, *Phys. Rev. Lett.* **98**, 076802 (2007).
- [63] E. Prodan, T. L. Hughes, and B. A. Bernevig, Entanglement Spectrum of a Disordered Topological Chern Insulator, *Phys. Rev. Lett.* **105**, 115501 (2010).
- [64] J. Li, R.-L. Chu, J. K. Jain, and S.-Q. Shen, Topological Anderson Insulator, *Phys. Rev. Lett.* **102**, 136806 (2009).
- [65] C. W. Groth, M. Wimmer, A. R. Akhmerov, J. Tworzydło, and C. W. J. Beenakker, Theory of the Topological Anderson Insulator, *Phys. Rev. Lett.* **103**, 196805 (2009).
- [66] H.-M. Guo, G. Rosenberg, G. Refael, and M. Franz, Topological Anderson Insulator in Three Dimensions, *Phys. Rev. Lett.* **105**, 216601 (2010).
- [67] L. Diósi, Continuous quantum measurement and Itô formalism, *Phys. Lett. A* **129**, 419 (1988).
- [68] A. Barchielli and V. P. Belavkin, Measurements continuous in time and a posteriori states in quantum mechanics, *J. Phys. A: Math. Gen.* **24**, 1495 (1991).
- [69] A. Barchielli and M. Gregoratti, *Quantum Trajectories and Measurements in Continuous Time* (Springer, Berlin, 2009).
- [70] I. Semina, V. Semin, F. Petruccione, and A. Barchielli, Stochastic Schrödinger equations for Markovian and non-Markovian cases, *Open Sys. Inf. Dyn.* **21**, 1440008 (2014).
- [71] G. Lindblad, On the generators of quantum dynamical semigroups, *Commun. Math. Phys.* **48**, 119 (1976).
- [72] C. Gardiner and P. Zoller, *Quantum Noise* (Springer, Berlin, 2004).
- [73] B.-Z. Wang, Y.-H. Lu, W. Sun, S. Chen, Y. Deng, and X.-J. Liu, Dirac-, Rashba-, and Weyl-type spin-orbit couplings: Toward experimental realization in ultracold atoms, *Phys. Rev. A* **97**, 011605(R) (2018).
- [74] W. Sun, B.-Z. Wang, X.-T. Xu, C.-R. Yi, L. Zhang, Z. Wu, Y. Deng, X.-J. Liu, S. Chen, and J.-W. Pan, Highly Controllable and Robust 2D Spin-Orbit Coupling for Quantum Gases, *Phys. Rev. Lett.* **121**, 150401 (2018).
- [75] In real experiments, the rescaled dynamical spin polarization can be constructed from the coefficients  $s_\alpha$ , oscillation frequency  $\omega$ , and decay rates  $\lambda_{0,1}$ , obtained by fitting the experimental data via Eq. (5).
- [76] The experiment following this theory is ongoing, and the sweet spot region is observed in the preliminary experiment.